









PAPER

[View Article Online](#)
[View Journal](#) | [View Issue](#)Cite this: *Catal. Sci. Technol.*, 2022,
12, 5861

From ethene to propene (ETP) on tailored silica–alumina supports with isolated Ni(II) sites: uncovering the importance of surface nickel aluminate sites and the carbon-pool mechanism†

Zixuan Chen, ^a Scott R. Docherty, ^b Pierre Florian, ^c
Agnieszka Kierzkowska, ^a Ilia B. Moroz, ^b Paula M. Abdala, ^a
Christophe Copéret, ^{*b} Christoph R. Müller ^{*a} and Alexey Fedorov ^{*a}

Catalysts with well-defined isolated Ni(II) surface sites have been prepared on three silica-based supports. The outer shells of the support were comprised either of an amorphous aluminosilicate or amorphous alumina (AlO_x) layer – associated with a high and low density of strong Brønsted acid sites (BAS), respectively. When tested for ethene-to-propene conversion, Ni catalysts with a higher density of strong BAS demonstrate a higher initial activity and productivity to propene. On all three catalysts, the propene productivity correlates closely with the concentration of C₈ aromatics, suggesting that propene may form via a carbon-pool mechanism. While all three catalysts deactivate with time on stream, the deactivation of catalysts with Ni(II) sites on AlO_x, *i.e.*, containing surface Ni aluminate sites, is shown to be reversible by calcination (coke removal), in contrast to the deactivation of surface Ni silicate or aluminosilicate sites, which deactivate irreversibly by forming Ni nanoparticles.

Received 18th July 2022,
Accepted 22nd August 2022

DOI: 10.1039/d2cy01272c

rsc.li/catalysis

Introduction

The development of processes for the on-purpose production of propene has been spurred in recent decades by the constantly growing demand for this important platform chemical.^{1,2} Such processes include, for instance, propane dehydrogenation^{3,4} or methanol-to-propene conversion.^{5–7} An appealing alternative route is the direct conversion of ethene to propene, *i.e.* the ETP reaction, which to date is still underdeveloped despite its advantages (mild reaction conditions and potentially atom economy).⁸ ETP catalysts based on zeolites and Al₂O₃-supported tungsten hydride have been reported.^{9–11} Ni-based ETP catalysts have also been developed, such as Ni ions on mesoporous silica, *i.e.* Ni-MCM-41,^{12–17} or on the Al-doped mesoporous support, Ni-Al-MCM-41.¹⁸ The presence of Al ions induced strong Brønsted acidity of the support and was found to increase the catalytic activity.¹⁸ Subsequently, ETP activity has been demonstrated for Ni-based catalysts on a non-mesoporous support, *i.e.*, Al-

doped silica,¹⁹ and the formation of propene starting from ethanol has been reported as well.^{20,21} Both isolated sites of Ni(II) and strong Brønsted acidity, arising from the introduction of Al, are thought to be essential for the ETP reaction to proceed.²² Despite those advances and mechanistic insights,²³ a detailed understanding of how strong Brønsted acidity influences the catalytic performance of Ni(II) sites in the ETP reaction is still lacking.

Atomic layer deposition (ALD) is a versatile approach to prepare supports with well-controlled surface acidity properties.^{24,25} Here, we utilize ALD of trimethylaluminum on partially dehydroxylated silica to prepare tailored non-mesoporous silica–alumina supports with a controlled density of strong Brønsted acid sites (BAS).²⁶ We then employ the surface organometallic chemistry (SOMC) approach to obtain isolated Ni(II) sites on those supports.^{22,27} We prepare three catalysts, study their ETP activity and productivity to propene and correlate it to the abundance of strong Brønsted acidity, which scales from high to medium and low depending on the number of ALD cycles (1, 5 and 10, respectively).²⁶ A detailed product analysis identifies that along with C₁–C₄ hydrocarbons, which are typical products of the Ni-based ETP reaction, a number of aromatic products form as well, including benzene, toluene, xylenes and ethylbenzene (denoted BTXE). We find that the formation rate of propene correlates closely with the formation rate of C₈ aromatics, in particular xylenes. This

^a Laboratory of Energy Science and Engineering, ETH Zürich, 8092 Zürich, Switzerland. E-mail: muelchri@ethz.ch, fedorooal@ethz.ch^b Department of Chemistry and Applied Biosciences, ETH Zürich, 8093 Zürich, Switzerland. E-mail: ccoperet@ethz.ch^c CNRS, CEMHTI UPR3079, University of Orléans, F-45071 Orléans, France† Electronic supplementary information (ESI) available. See DOI: <https://doi.org/10.1039/d2cy01272c>

observation is consistent with the cracking of ethene oligomers, produced by the Ni(II) sites, on cationic C₈ species (such as xylenes protonated by the strong BAS). In other words, a carbon-pool mechanism is likely responsible for the propene production on Ni-based ETP catalysts containing strong Brønsted acidity; such a pathway is reminiscent of that involved in zeolite-catalyzed ETP conversion,^{28,29} and also in the methanol-to-olefins process.^{30,31}

Importantly, we also uncover that the use of supports that contain an amorphous alumina (AlO_x) overlayer yields catalysts that avoid the formation of nickel nanoparticles (NPs) from isolated Ni(II) sites with time on stream (TOS); the latter is a typical deactivation pathway of Ni-based ETP catalysts. The formation of surface nickel aluminate sites on the AlO_x overlayer is proposed to be responsible for the increased stability against deactivation by Ni NPs formation, which likely takes place by the reduction of Ni(II) sites to metallic Ni followed by sintering. In contrast, isolated nickel silicate or aluminosilicate sites form Ni NPs with TOS and therefore do not regenerate fully during coke removal *via* calcination, while the catalysts with isolated nickel aluminate sites regenerate fully by calcination. Therefore, a combination of strong Brønsted acidity and isolated nickel aluminate sites is proposed to be essential features of active Ni-based ETP catalysts amenable to complete regeneration, while propene is proposed to form, at least in part, *via* a carbon-pool mechanism.

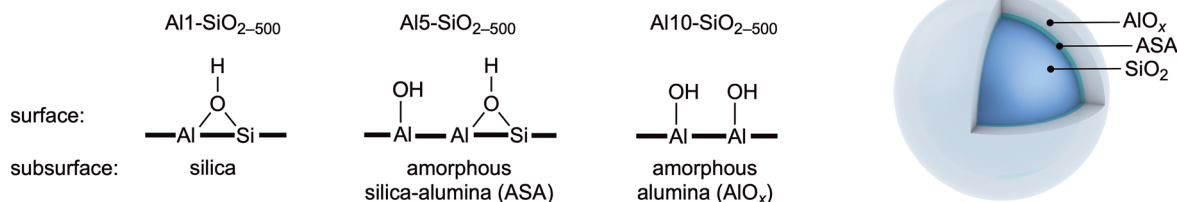
Results

ALD-derived silica–alumina supports with a controlled abundance of strong Brønsted acid sites were prepared using

1, 5 or 10 ALD cycles of trimethylaluminum onto silica dehydroxylated at 500 °C, as described by us previously.²⁶ This methodology yields supports with a high, medium and low abundance of strong Brønsted acidity. Depending on the number of cycles, the respective materials are denoted Al1-SiO₂₋₅₀₀, Al5-SiO₂₋₅₀₀ and Al10-SiO₂₋₅₀₀ and their surface area ranges between 280 and 160 m² g⁻¹. According to our previous detailed solid state NMR studies, the ALD-deposited shell (with a silica core) in Al1-SiO₂₋₅₀₀ is an amorphous aluminosilicate (ASA), which contains abundant strong BAS.²⁶ In contrast, Al5-SiO₂₋₅₀₀ and Al10-SiO₂₋₅₀₀ contain layers of AlO_x grown on top of the ASA shell (Fig. 1).²⁶ With respect to Al1-SiO₂₋₅₀₀, the amorphous alumina shell in Al5-SiO₂₋₅₀₀ features a decreased abundance of strong BAS; in Al10-SiO₂₋₅₀₀ the abundance of strong BAS is reduced further. Using these supports, three ETP catalysts containing isolated Ni(II) sites were prepared by the SOMC approach.²⁷ This approach relies on a selective reaction between surface sites of a dehydroxylated support (such as isolated silanol or aluminol OH groups) and a molecular complex, *viz.* a grafting reaction, which in our case is a siloxide ligand exchange reaction between [Ni(OSi(O^tBu)₃)₂]₂ and the surface hydroxyl groups of the Al1,5,10-SiO₂₋₅₀₀ supports dehydroxylated at 500 °C (Fig. 1).²² Following the grafting reaction, the materials are calcined at 400 °C (see ESI† for details) similarly to our previous report,²² and characterized avoiding exposure to air. Henceforth, the three catalysts prepared are denoted Ni-Al1-, Ni-Al5-, Ni-Al10-SiO₂₋₅₀₀ and contain, according to elemental analysis, 0.73%, 1.03%, 1.09 wt% Ni, respectively.

A detailed characterization of the prepared catalysts is reported in the ESI†. In brief, the application of the

ALD-derived supports with a controlled density of strong BAS



Synthesis of Ni-Al-SiO₂₋₅₀₀ ETP catalysts

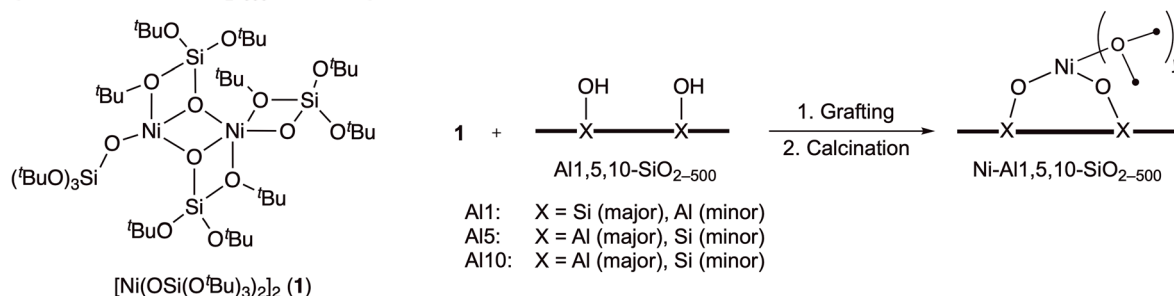


Fig. 1 The ALD-SOMC approach to yield catalysts with isolated Ni(II) sites on the ALD-derived alumina–silica supports with a controlled density of strong Brønsted acid sites. The notations AlO_x and ASA refer to amorphous alumina and amorphous silica–alumina (an aluminosilicate layer), respectively. The structure of the calcined Ni-Al-SiO₂₋₅₀₀ catalysts is shown with X = Al and Si assuming a mono-grafting of [Ni(OSi(O^tBu)₃)₂]₂ on Al1-, Al5- and Al10-SiO₂₋₅₀₀ supports, and that the calcination of the mono-grafted species may, at least partially, proceed without breaking the Ni–O–Si linkage. See Table 1 for the possible range of values of variable *y*.



combined ALD-SOMC approach yields materials that contain isolated Ni(II) sites supported on Al_{1,5,10}-SiO₂₋₅₀₀. X-ray absorption near-edge structure (XANES) data suggests a Ni(II) oxidation state in all three catalysts (Fig. S8†). The results of the extended X-ray absorption fine structure (EXAFS) analysis of all three materials reveal the presence of Ni–O and Ni–Al(Si) coordination spheres and are indicative of the presence of isolated Ni(II) sites. The EXAFS data were fitted using Ni–O and Ni–Al/Si paths and the fitting parameters are summarized in Table 1.³² All three Ni-Al_{1,5,10}-SiO₂₋₅₀₀ catalysts exhibit two similar coordination spheres in EXAFS. The first coordination sphere is represented by a single Ni–O path while the second coordination sphere is fitted with two Ni–Al(Si) paths at two different interatomic distances. As discussed above, Al₁-SiO₂₋₅₀₀ support is different from Al₅- and Al₁₀-SiO₂₋₅₀₀ supports in that Al₁-SiO₂₋₅₀₀ has an amorphous aluminosilicate (ASA) shell while Al₅- and Al₁₀-SiO₂₋₅₀₀ supports contain an amorphous alumina (AlO_x) shell. Therefore, it is challenging to distinguish between Ni–Si and Ni–Al paths in Ni-Al₁-SiO₂₋₅₀₀ as the atomic number of Si and Al are close.^{33,34} It is likely that both Ni–Si and Ni–Al paths are present in Ni-Al₁-SiO₂₋₅₀₀ while Ni–Al paths dominate the second sphere in Ni-Al₅-SiO₂₋₅₀₀ and Ni-Al₁₀-SiO₂₋₅₀₀ (Fig. S9–S11†). The presence of a Ni–Ni second coordination sphere can be ruled out (see ESI† for additional discussion), hence excluding the possibility of the formation of NiO crystallites (Tables S1 and S2, Fig. S12†). In line with the EXAFS analysis, the characteristic feature of NiO at *ca.* 8370 eV is absent in the XANES spectra of all three Ni-Al_{1,5,10}-SiO₂₋₅₀₀ catalysts. In Ni-Al₁-SiO₂₋₅₀₀, the Ni sites are likely a combination of both surface nickel silicate and nickel aluminate sites, while in Ni-Al₅-SiO₂₋₅₀₀ and Ni-Al₁₀-SiO₂₋₅₀₀ these are predominantly nickel aluminate sites.

The ²⁷Al nuclear magnetic resonance (NMR) spectra of Ni-Al₁, Ni-Al₅-, Ni-Al₁₀-SiO₂₋₅₀₀ display features similar to those of Al₁-, Al₅-, and Al₁₀-SiO₂₋₅₀₀ reported by us previously,²⁶ *i.e.*, the spectra contain three overlapping peaks due to four-, five- and six-fold coordinated Al sites (Fig. S36†). The chemical shifts are found to increase with increasing number of ALD cycles, explained by more abundant Al–O–Al linkages (in preference to Al–O–Si linkages). Compared to the spectra of Al₁-, Al₅-, and Al₁₀-SiO₂₋₅₀₀, there is a significant increase of

the line width in Ni-Al₁-, Ni-Al₅- and Ni-Al₁₀-SiO₂₋₅₀₀ due to a larger distribution of the isotropic chemical shift values $\Delta\delta_{\text{iso}}$ (Fig. S36, Table S4†). This points at an increased chemical disorder in the Ni catalysts, likely caused by the SOMC deposition and calcination steps.

Note that a paramagnetic Ni(II) site in our catalysts “bleaches” nearby Al sites, making them invisible in the ²⁷Al NMR spectra. The normalized (with respect to the weight and the number of scans), integrated area of the NMR peaks is found to be 0.95, 4.58 and 9.77 a.u. for Ni-Al₁-, Ni-Al₅- and Ni-Al₁₀-SiO₂₋₅₀₀ respectively, which corresponds to a relative ratio of 1:4.8:10.3 of aluminum atoms in the samples detected by NMR. This ratio is very close to the number of ALD cycles used (*i.e.*, 1, 5 and 10 cycles). In other words, the spatial distribution of Ni and the effect of paramagnetic bleaching is homogeneous for all three samples and no Ni clustering is evidenced by NMR, in agreement with the EXAFS data. Next, we fitted the ²⁷Al NMR spectra of Ni-Al₅- and Ni-Al₁₀-SiO₂₋₅₀₀ using the spectrum of Ni-Al₁-SiO₂₋₅₀₀ as a model of the SiO₂–AlO_x interface. The bleaching effect of Ni(II) explains the lower fitted fraction of the Ni-Al₁-SiO₂₋₅₀₀ component in Ni-Al₅-SiO₂₋₅₀₀ relative to Al₅-SiO₂₋₅₀₀ (21% and 51%, respectively, Table S4†; the SiO₂–AlO_x interface has been modelled in Al₅-SiO₂₋₅₀₀ and Al₁₀-SiO₂₋₅₀₀ using the spectrum of Al₁-SiO₂₋₅₀₀).²⁶ The same effect is observed in Ni-Al₁₀-SiO₂₋₅₀₀ relative to Al₁₀-SiO₂₋₅₀₀ (30% and 37%, respectively), although it is notably less pronounced. Therefore, the differences in the fitting results of the Ni-Al₁-SiO₂₋₅₀₀ component suggest that in Ni-Al₅-SiO₂₋₅₀₀ a large fraction of the Ni(II) sites are located in the vicinity of the strong BAS of the SiO₂–AlO_x interface, yet this is not the case in Ni-Al₁₀-SiO₂₋₅₀₀.

FTIR studies using pyridine (Py) as the probe molecule show that bands due to the pyridinium ion (Py protonated by strong BAS) are observed clearly in Ni-Al₁-SiO₂₋₅₀₀, while they are less intense in Ni-Al₅-SiO₂₋₅₀₀ and nearly not discernable in Ni-Al₁₀-SiO₂₋₅₀₀ (Fig. S13†). Those results are consistent with the degree of abundance of strong BAS in the respective Al₁-, Al₅- and Al₁₀-SiO₂₋₅₀₀ supports as discussed above.²⁶ However, an additional Lewis acid site (LAS) emerges in Ni-Al_{1,5,10}-SiO₂₋₅₀₀ materials, identified by an adsorbed Py band at 1614 cm^{−1} that is lacking in Al_{1,5,10}-SiO₂₋₅₀₀ supports. This band is ascribed to Py coordinated to isolated Ni(II) sites (see ESI† for additional discussion).

Table 1 Fits of the structural parameters obtained from the Ni K-edge EXAFS data

Material	Neighbour	CN	<i>r</i> (Å)	σ^2 (Å ²)	<i>E</i> ₀ (eV)	<i>R</i> -Factor
Ni-Al ₁ -SiO ₂₋₅₀₀	O	4.8(4)	2.00(3)	0.009(1)	−4(1)	0.002
	Si(Al)	1.5(3)	2.78(8)	0.009(1)		
	Al(Si)	2.1(4)	3.22(7)	0.009(1)		
Ni-Al ₅ -SiO ₂₋₅₀₀	O	4.9(7)	1.98(6)	0.009(1)	−8(2)	0.005
	Al(Si)	1.1(5)	2.77(9)	0.009(1)		
	Al	2.1(6)	3.19(9)	0.009(1)		
Ni-Al ₁₀ -SiO ₂₋₅₀₀	O	4.4(4)	1.99(4)	0.008(1)	−5(1)	0.002
	Al(Si)	1.0(3)	2.76(9)	0.008(1)		
	Al	1.7(4)	3.22(7)	0.008(1)		

All samples were measured at ambient temperature. *S*₀² was fixed to 0.847 obtained by fitting a Ni foil reference. CN stands for the coordination number. Debye–Waller factor σ^2 were constrained to the same value for all paths in each sample.



The catalytic performance of the prepared Ni–Al catalysts was assessed by flowing 10% C₂H₄/N₂ through a catalyst bed that was kept at 350 °C (space velocity was 200 mL g_{cat}^{−1} h^{−1}). While all three catalysts are active for ETP, their initial activity, stability with TOS and distribution of products differ significantly (Table 2). Ni–Al1–SiO₂₋₅₀₀, a material with the most abundant strong BAS, converts ethene notably faster than Ni–Al5–SiO₂₋₅₀₀ and Ni–Al10–SiO₂₋₅₀₀ catalysts; the respective initial (at TOS = 7 min) consumption rates of ethene are 16.8, 5.9 and 6.4 g(C₂H₄) g_{Ni}^{−1} h^{−1} obtained at 55%, 20% and 30% conversion, respectively (Table 2, Fig. S14†). Interestingly, in contrast to Ni–Al1–SiO₂₋₅₀₀ and Ni–Al10–SiO₂₋₅₀₀, Ni–Al5–SiO₂₋₅₀₀ displays an activation period (*ca.* 150 min) associated with an increase of ethene conversion from *ca.* 20% to 25%, before deactivation sets in. Possible reasons for the activation period of Ni–Al5–SiO₂₋₅₀₀ are discussed below. Deactivation with TOS is observed for all three catalysts. After 20 h TOS, the conversion of Ni–Al1-, Ni–Al5- and Ni–Al10–SiO₂₋₅₀₀ decreases to only 8%, 10% and 3% of the initial values, respectively. The initial productivity to propene on Ni–Al1–SiO₂₋₅₀₀ is 2.7 g(C₃H₆) g_{Ni}^{−1} h^{−1}, followed by Ni–Al10–SiO₂₋₅₀₀ and Ni–Al5–SiO₂₋₅₀₀ (0.6 and 0.2 g(C₃H₆) g_{Ni}^{−1} h^{−1}, respectively). However, the productivity to propene raises after 150 min TOS for Ni–Al5–SiO₂₋₅₀₀ (due to an activation period mentioned above) reaching *ca.* 0.8 g(C₃H₆) g_{Ni}^{−1} h^{−1}.

Butenes (1-butene, *iso*-butene, *trans*- and *cis*-2-butene) are formed on all three catalysts, consistent with the dimerization of ethene to 1-butene on the isolated Ni(II) sites followed by isomerization reactions (Fig. S16–S18†). In addition to olefins, the Ni–Al–SiO₂₋₅₀₀ catalysts produce C₁–C₄ alkanes, in particular ethane, whereby the partial selectivity to ethane among the C₁–C₄ alkanes exceeds 85% (Fig. S21†). The productivity to alkanes is especially high at short TOS, suggesting the formation of hydrogen (*via* coking) and its use for the hydrogenation of alkenes and, possibly, hydrogenolysis of alkanes. For instance, at TOS = 50 min, the productivity to C₁–C₄ alkanes is 0.79, 0.52 and 0.30 g(alkanes) g_{Ni}^{−1} h^{−1} for Ni–Al1-, Ni–Al5- and Ni–Al10–SiO₂₋₅₀₀, respectively (Fig. S20†). At TOS = *ca.* 1 h the productivity to alkanes starts to decrease for all three catalysts, before ceasing after TOS = *ca.* 10 h (Table 2, Fig. S16–S18†).

The initial carbon balance on Ni–Al1-, Ni–Al5-, and Ni–Al10–SiO₂₋₅₀₀ is only 80%, 88% and 89%, respectively. However, after 10 h on stream, all three catalysts reach *ca.* 100% carbon balance (Table 2, Fig. S16–S18†). The low initial carbon balance indicates the formation of non-volatile hydrocarbons and coke. Coking is also evidenced by the

change of color of the Ni–Al–SiO₂₋₅₀₀ catalysts from pale-grey to black after the catalytic tests and is consistent with the increase of the catalyst mass observed during *in situ* TGA experiments (Fig. S33†). In addition, Raman spectra of spent Ni–Al catalysts reveal two main peaks centered at *ca.* 1350 cm^{−1} and 1580 cm^{−1}, ascribed to the disordered carbon and ordered graphitic lattice, respectively (Fig. S32†).³⁵ The ratio between these peaks, *i.e.*, the D₁/G area ratio, is used to evaluate the degree of disorder in the graphitic coke deposits. While similar D₁/G ratio of 1.5 was obtained for Ni–Al1–SiO₂₋₅₀₀ and Ni–Al5–SiO₂₋₅₀₀, Ni–Al10–SiO₂₋₅₀₀ features a lower D₁/G ratio of 0.3 (see ESI† for further details). The evolution of the productivity to alkanes with TOS correlates closely with that of coking (evaluated by the carbon balance) and the formation of H₂ (Fig. S20†).

Interestingly, aromatic products (benzene, toluene, xylenes, ethylbenzene, BTX) form on all three Ni–Al–SiO₂₋₅₀₀ catalysts. Ni–Al1–SiO₂₋₅₀₀ exhibits the highest productivities to toluene and C₈ aromatics (ethylbenzene and *o*-, *m*-, *p*-xylene) whereas Ni–Al10–SiO₂₋₅₀₀ produces predominantly benzene at TOS = 7 min (Fig. S19†).³⁶ After TOS = 8 h, the partial selectivity (*i.e.*, the selectivity among aromatic products) to C₈ aromatics is more than 60% on all three catalysts. Control experiments show that the respective supports Al1-, Al5-, and Al10–SiO₂₋₅₀₀ do not catalyze ETP, nor do they form any aromatic products (Fig. S30†). The initial ethene conversion on these supports does not exceed 5% and is likely due to the formation of coke.

To understand the nature of the surface species formed during the ETP experiment, Ni–Al5–SiO₂₋₅₀₀ was heated with a 1:1 mixture of ¹³C₂H₄/C₂H₄ at 350 °C for 12 h. The subsequently acquired ¹³C CP-MAS spectrum of the resulted black solid shows two major peaks in the range 110–150 ppm and 10–40 ppm, assigned to aromatic carbonaceous species and aliphatic groups, respectively (Fig. S38†). The presence of such species has been ascribed previously to the formation of alkylated aromatic hydrocarbons in zeolites,^{37–39} and in other alumina-based catalysts.⁴⁰ Furthermore, comparing the ¹H spin-echo spectra of Ni–Al5–SiO₂₋₅₀₀ after exposure to ¹³C₂H₄/C₂H₄ (350 °C, 12 h) with that of fresh Ni–Al5–SiO₂₋₅₀₀, confirms the emergence of peaks at *ca.* 2 ppm and 7 ppm, consistent with benzylic and aromatic protons, respectively (Fig. S39†); the peak at *ca.* 21 ppm in ¹³C NMR spectrum further suggests the presence of Ar–CH₃ benzylic groups (Fig. S38†). Notably, no additional signals are observed in the range 4–6 ppm, ruling out the presence of adsorbed olefinic species (*i.e.* ethene, propene, butenes, *etc.*). Analysis of the gas phase of

Table 2 Results of ICP analysis and catalytic tests. Catalytic data is presented after 7 min TOS and, in parentheses, after 20 h TOS

Entry	Catalyst	Ni content (wt%)	Ethene conversion (%)	Propene productivity (g g _{Ni} ^{−1} h ^{−1})	C ₄ olefins productivity (g g _{Ni} ^{−1} h ^{−1})	C ₁ –C ₄ alkane productivity (g g _{Ni} ^{−1} h ^{−1})	H ₂ productivity (g g _{Ni} ^{−1} h ^{−1})	Carbon balance (%)
1	Ni–Al1–SiO ₂₋₅₀₀	0.73	55 (8)	2.7 (0.6)	5.5 (1.8)	1.1 (0.1)	0.16 (0.005)	80 (100)
2	Ni–Al5–SiO ₂₋₅₀₀	1.03	20 (10)	0.2 (0.5)	0.3 (1.3)	0.2 (0.1)	0.03 (0.003)	88 (100)
3	Ni–Al10–SiO ₂₋₅₀₀	1.09	30 (3)	0.6 (0.1)	1.7 (0.4)	0.4 (0.1)	0.02 (0.004)	89 (100)



the batch experiment by GC-MS confirms the formation of a statistical mixture of ^{13}C isotopologues of propene (Fig. S41, Table S6†). In addition to propene, ethane is detected and its formation is explained by the hydrogenation of ethene by H_2 (formed due to coking) over the course of the experiment. However, in contrast to propene, ethane features mostly a mixture of unlabelled and di-labelled isotopologues with only a small amount (*ca.* 5%) of the mono-labelled isotopologue (Fig. S40, Table S5†). This result is inconsistent with the presence of olefin metathesis based ETP mechanism that has been proposed previously for Ni-based catalysts,¹² and is in line with the cracking pathways.²³

Transmission electron microscopy (TEM) imaging and energy dispersive X-ray (EDX) mapping of spent Ni-Al1-SiO₂₋₅₀₀ (*i.e.*, after 20 h TOS) reveal the formation of Ni NPs (Fig. S22†). This is explained by the evolution of Ni(II) sites to reduced Ni species under reaction conditions, their degrafting (dissociation) from the support and agglomeration to Ni NPs (either metallic Ni, carburized Ni, or a mixture of thereof). Note that no Ni NPs are observed in any of the fresh catalysts (Fig. S4–S6†). Interestingly, in contrast to Ni-Al1-SiO₂₋₅₀₀, no Ni NPs are found in spent Ni-Al5-SiO₂₋₅₀₀ and Ni-Al10-SiO₂₋₅₀₀; EDX mappings show that the Ni sites remain

homogeneously distributed on Ni-Al5-SiO₂₋₅₀₀ and Ni-Al10-SiO₂₋₅₀₀ after the 20 h catalytic test (Fig. S23 and S24†). Our observations, *i.e.* the formation of coke and the retention of isolated Ni sites on deactivated Ni-Al5-SiO₂₋₅₀₀ and Ni-Al10-SiO₂₋₅₀₀ catalysts, suggest that regeneration of the initial activity by calcination should be viable for these two catalysts.

To test this hypothesis, the reaction-regeneration cycles were carried out by passing synthetic air at 500 °C for 1 h (to remove coke) through the catalyst bed that has been exposed for 5 h to ETP conditions. No substantial changes in the productivity of propene (except for the increased propene productivity after the first regeneration cycle for Ni-Al5-SiO₂₋₅₀₀, *vide infra*) were observed between the first, second and indeed up to the fifth regeneration cycle for Ni-Al5-SiO₂₋₅₀₀ and Ni-Al10-SiO₂₋₅₀₀, suggesting that these catalysts can be fully regenerated (Fig. 2). However, regeneration of Ni-Al1-SiO₂₋₅₀₀ could restore the propene productivity of the previous cycles only partially. Those observations further confirm the differences in the deactivation mechanisms between Ni-Al1-SiO₂₋₅₀₀ on one hand and Ni-Al5- and Ni-Al10-SiO₂₋₅₀₀ on the other hand, consistent with the TEM results. In other words, two deactivation pathways proceed in Ni-Al1-SiO₂₋₅₀₀ during ETP, *i.e.* (i) the formation of Ni NPs due to the reduction of

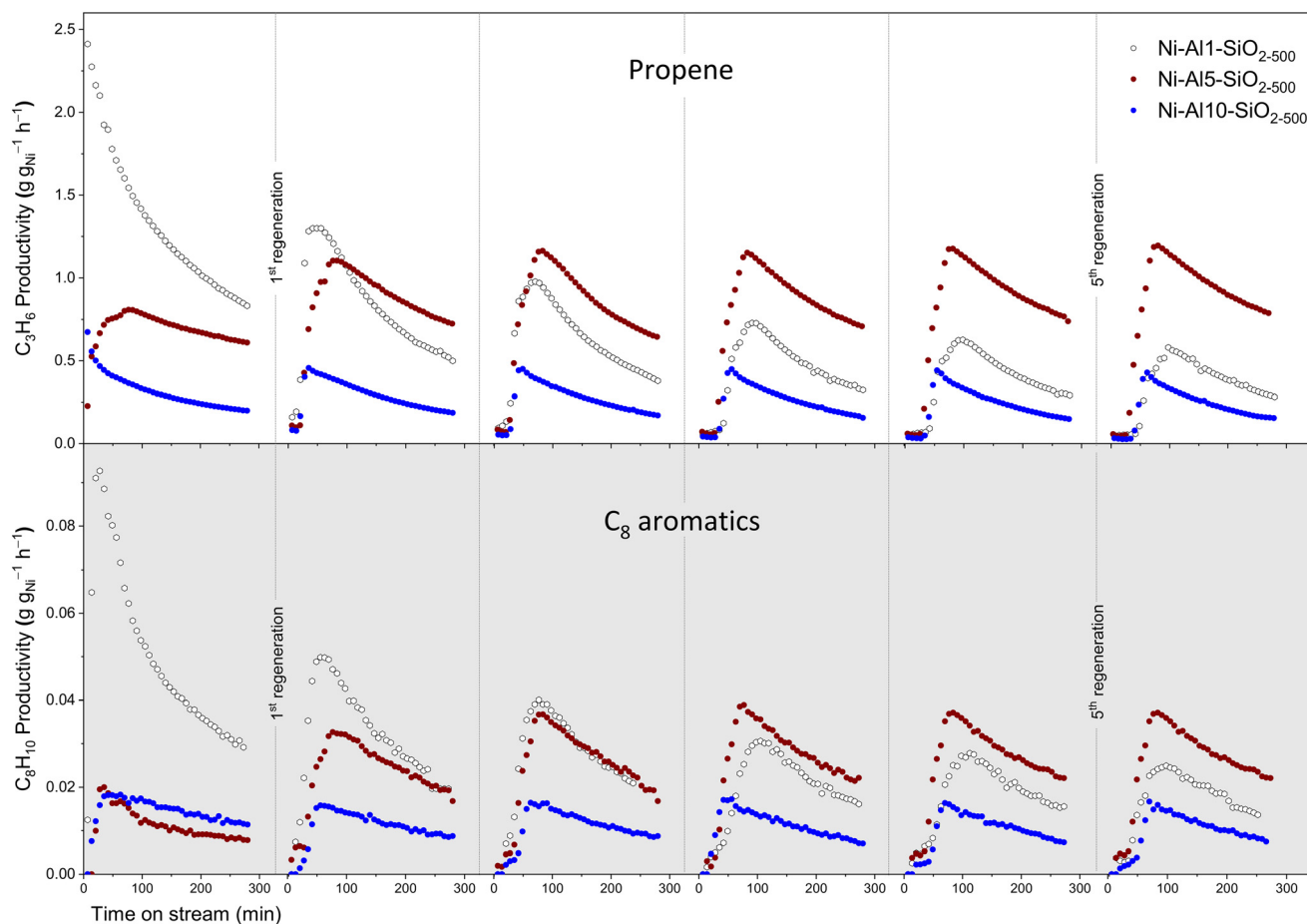


Fig. 2 The productivity to propene and C₈ aromatics (ethylbenzene and o-, m-, p-xylene) on Ni-Al1-, Ni-Al5- and Ni-Al10-SiO₂₋₅₀₀ catalysts (black-and-white, red and blue symbols, respectively) over in total 30 h TOS including five regeneration cycles (after every 5 h TOS).



Ni(II) single sites and the agglomeration of the reduced species (see above, Fig. S22†) and (ii) coke deposition. While coke can be removed by calcination, the oxidation of the agglomerated Ni NPs gives NiO, which, in contrast to isolated sites of Ni(II), does not catalyze the oligomerization of ethene efficiently. In contrast, the Ni-Al5- and Ni-Al10-SiO₂₋₅₀₀ catalysts deactivate only by coke deposition (*i.e.*, blocking of the active sites by coke) since their catalytic activity is fully recovered after regeneration by calcination.

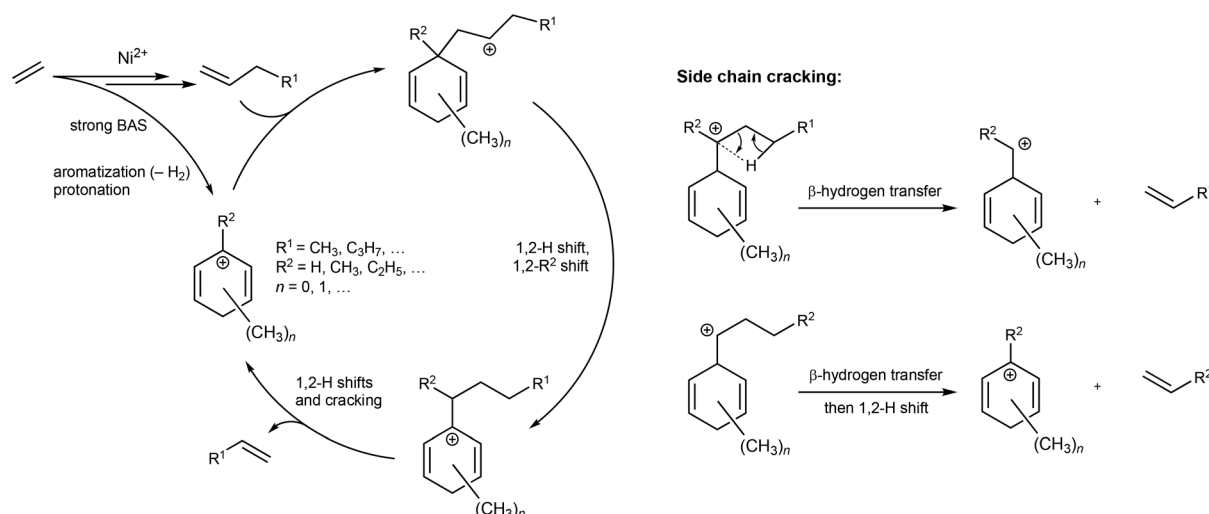
Interestingly, after the first regeneration cycle, Ni-Al5-SiO₂₋₅₀₀ displays a propene productivity that is increased by *ca.* 30% and which is maintained in every subsequent ETP-regeneration cycle (Fig. 2). We note that the temperature used for regeneration is higher relative to the initial calcination temperature of the grafted Ni species (500 °C and 400 °C, respectively). This higher temperature is required because coke removal is incomplete at 400 °C, and as a result, a longer activation period and a lower maximum propene productivity is observed if a regeneration temperature of 400 °C is used instead of a regeneration temperature of 500 °C (Fig. S34†). However, if Ni-Al5-SiO₂₋₅₀₀ is prepared by calcination of the grafted Ni species at 500 °C, the resulted propene productivities of the fresh and the regenerated catalysts are similar (Fig. S31†). Therefore, the observed increase by *ca.* 30% in the propene productivity of Ni-Al5-SiO₂₋₅₀₀ may be due to a structural evolution of Ni-Al5-SiO₂₋₅₀₀ at 500 °C.

To probe for possible structural changes of Ni-Al5-SiO₂₋₅₀₀ during the regeneration process, we have applied ²⁷Al MAS NMR spectroscopy. The narrower spectral lines in Ni-Al5-SiO_{2-500-regen} reveal a higher structural ordering in this material, yet the lines become also narrower in the Ni-free reference Al5-SiO_{2-500-regen} (Fig. S37†). In addition, the relative fractions of ⁴Al/⁵Al/⁶Al sites change in both Ni-Al5-SiO_{2-500-regen} and Al5-SiO_{2-500-regen} (Table S4†). The modelling of Ni-Al5-SiO_{2-500-regen} shows smaller $\Delta\delta_{\text{iso}}$ and \bar{C}_Q than in fresh Ni-Al5-SiO₂₋₅₀₀ (both modellings use three Al sites). In addition, a shift of δ_{iso} towards higher chemical shifts and a decreased proportion of four-coordinated

aluminum environments is observed after regeneration. This points to a complex mechanism for the structural reorganization during regeneration involving not only the OH groups (usually at the origin of the coordination increase), but also the chemical Al/Si mixing, which drives changes in δ_{iso} .²⁶ Differences in the NMR parameters of Al5-SiO_{2-500-regen} and Ni-Al5-SiO_{2-500-regen} show that Ni also plays a role in the structural ordering of the catalysts during regeneration.

The activation time that lasts *ca.* 50–100 min is observed in all Ni-Al-SiO₂₋₅₀₀ catalysts following regeneration; in addition, fresh Ni-Al5-SiO₂₋₅₀₀ features an activation period as well. After 90 min TOS, following the sixth regeneration, *i.e.* close to the highest propene productivity, the three Ni-Al catalysts were collected and FTIR spectra were recorded without exposure to air. The spectra of fresh and regenerated catalysts after 90 min TOS are similar (Fig. S25†). That being said, the comparison between the Py-FTIR spectra of fresh and regenerated Ni-Al5-SiO₂₋₅₀₀ catalysts reveals a decreased relative intensity of the IR band corresponding to the Lewis acidic Ni(II) sites as compared to the intensity of Py on the Al-based LAS on the regenerated catalysts (Fig. S35†). This result suggests that restructuring of the catalyst surface after calcination may occur with TOS, although more studies are needed to understand details of this process. Lastly, TEM images and EDX mapping of the activated and spent Ni-Al-SiO₂₋₅₀₀ catalysts are also similar, *i.e.* Ni NPs are only observed in activated and spent Ni-Al1-SiO₂₋₅₀₀ and not observed in Ni-Al5-SiO₂₋₅₀₀ and Ni-Al10-SiO₂₋₅₀₀ (Fig. S27–S29†).

Interestingly, comparing changes in the productivity to aromatic products with TOS, in particular C₈ aromatics, with changes in the productivity to propene reveal a very clear correlation (Fig. 2 and S15†). For instance, the continuously decreasing propene productivity on Ni-Al1-SiO₂₋₅₀₀ with every additional regeneration cycle correlates closely with the decreasing productivity to C₈ aromatics. This result suggests that the formation of propene may involve the intermediacy of alkylated aromatics (and, possibly, *vice versa*). The results



discussed above are consistent with the following reaction mechanism. Ethene is first dimerized to 1-butene and then oligomerized further on Ni(II) sites,⁴¹ whereas strong BAS catalyze olefin aromatization to BTXE,⁴² and provide protonated aromatic species that can be alkylated by olefins such as 1-butene. Cracking of the side chain of the resulting intermediates may form propene and regenerate the cationic aromatic species (Scheme 1). This carbon-pool mechanism is thus complementary to the ETP mechanisms proposed previously (chain growth on Ni sites and cracking of oligomers on the strong BAS),²² and is related to the pathways of the zeolite-catalyzed ETP reaction.^{28,29}

In conclusion, we have reported that Ni-based catalysts with abundant strong BAS show a higher propene productivity relative to catalysts with less abundant strong BAS. The role of the strong BAS is not only limited to the cracking of ethene oligomers, but they also catalyze the aromatization of ethene and higher olefins to BTXE products. When protonated, these aromatics can be further alkylated, which in turn facilitates the cracking process (*i.e.*, the carbon-pool mechanism). Lastly, the formation of Ni aluminate sites on the amorphous alumina overlayer prevents Ni(II) from overreduction which would lead to the formation of Ni nanoparticles. These findings expand the scope and understanding of Ni-based catalysts in the ETP reaction. Our future work will focus on the development of isolated Ni(II) sites that are stable under ETP conditions in the presence of abundant strong BAS. Moreover, kinetic studies will be needed to improve our understanding of the role of the cracking of linear oligomers *vs.* the cracking of alkylated aromatic species in the ETP reaction.

Conflicts of interest

There are no conflicts to declare.

Acknowledgements

We acknowledge Scientific Centre for Optical and Electron Microscopy (ScopeM, ETH Zürich) for providing access to electron microscopy facilities. Z. C. thanks ETH Zürich for financial support (ETH-40 17-2). S. R. D. and C. C. acknowledge the Swiss National Science Foundation (grants 200021_169134, 200020B_192050, and CRSII5_183495). The Swiss Norwegian Beamlines (SNBL) at European Synchrotron Facilities (ESRF) is acknowledged for providing access to the BM31 beamline. This publication was created as part of NCCR Catalysis (grant number 180544), a National Centre of Competence in Research funded by the Swiss National Science Foundation.

References

- 1 J. S. Plotkin, *Catal. Today*, 2005, **106**, 10–14.
- 2 H. A. Wittcoff, B. G. Reuben and J. S. Plotkin, *Industrial Organic Chemicals*, John Wiley & Sons, Inc., Hoboken, New Jersey, 2nd edn, 2004.
- 3 S. R. Docherty, L. Rochlitz, P. A. Payard and C. Copéret, *Chem. Soc. Rev.*, 2021, **50**, 5806–5822.
- 4 S. Chen, X. Chang, G. Sun, T. Zhang, Y. Xu, Y. Wang, C. Pei and J. Gong, *Chem. Soc. Rev.*, 2021, **50**, 3315–3354.
- 5 A. Galadima and O. Muraza, *Ind. Eng. Chem. Res.*, 2015, **54**, 4891–4905.
- 6 U. Olsbye, M. Bjørgen, S. Svelle, K.-P. Lillerud and S. Kolboe, *Catal. Today*, 2005, **106**, 108–111.
- 7 M. A. Ali, S. Ahmed, N. Al-Baghli, Z. Malaibari, A. Abutaleb and A. Yousef, *Catal. Lett.*, 2019, **149**, 3395–3424.
- 8 C. Copéret, F. Allouche, K. W. Chan, M. P. Conley, M. F. Delley, A. Fedorov, I. B. Moroz, V. Mougel, M. Pucino, K. Searles, K. Yamamoto and P. A. Zhizhko, *Angew. Chem., Int. Ed.*, 2018, **57**, 6398–6440.
- 9 B. Lin, Q. Zhang and Y. Wang, *Ind. Eng. Chem. Res.*, 2009, **48**, 10788–10795.
- 10 M. Taoufik, E. Le Roux, J. Thivolle-Cazat and J. M. Basset, *Angew. Chem., Int. Ed.*, 2007, **46**, 7202–7205.
- 11 E. Mazoyer, K. C. Szeto, N. Merle, J. Thivolle-Cazat, O. Boyron, J.-M. Basset, C. P. Nicholas and M. Taoufik, *J. Mol. Catal.*, 2014, **385**, 125–132.
- 12 M. Iwamoto and Y. Kosugi, *J. Phys. Chem. C*, 2007, **111**, 13–15.
- 13 K. Ikeda, Y. Kawamura, T. Yamamoto and M. Iwamoto, *Catal. Commun.*, 2008, **9**, 106–110.
- 14 T. Lehmann, T. Wolff, V. M. Zahn, P. Veit, C. Hamel and A. Seidel-Morgenstern, *Catal. Commun.*, 2011, **12**, 368–374.
- 15 A. S. Frey and O. Hinrichsen, *Microporous Mesoporous Mater.*, 2012, **164**, 164–171.
- 16 M. Tanaka, A. Itadani, Y. Kuroda and M. Iwamoto, *J. Phys. Chem. C*, 2012, **116**, 5664–5672.
- 17 T. Lehmann, T. Wolff, C. Hamel, P. Veit, B. Garke and A. Seidel-Morgenstern, *Microporous Mesoporous Mater.*, 2012, **151**, 113–125.
- 18 L. Alvarado Perea, T. Wolff, P. Veit, L. Hilfert, F. T. Edelmann, C. Hamel and A. Seidel-Morgenstern, *J. Catal.*, 2013, **305**, 154–168.
- 19 M. Stoyanova, M. Schneider, M.-M. Pohl and U. Rodemerck, *Catal. Commun.*, 2017, **92**, 65–69.
- 20 M. Iwamoto, K. Kasai and T. Haishi, *ChemSusChem*, 2011, **4**, 1055–1058.
- 21 M. Iwamoto, *Molecules*, 2011, **16**, 7844–7863.
- 22 I. B. Moroz, A. Lund, M. Kaushik, L. Severy, D. Gajan, A. Fedorov, A. Lesage and C. Copéret, *ACS Catal.*, 2019, **9**, 7476–7485.
- 23 U. Rodemerck, E. V. Kondratenko, M. Stoyanova and D. Linke, *J. Catal.*, 2020, **389**, 317–327.
- 24 A. R. Mouat, C. George, T. Kobayashi, M. Pruski, R. P. van Duyn, T. J. Marks and P. C. Stair, *Angew. Chem., Int. Ed.*, 2015, **54**, 13346–13351.
- 25 A. G. M. Rankin, P. B. Webb, D. M. Dawson, J. Viger-Gravel, B. J. Walder, L. Emsley and S. E. Ashbrook, *J. Phys. Chem. C*, 2017, **121**, 22977–22984.
- 26 M. Kaushik, C. Leroy, Z. Chen, D. Gajan, E. Willinger, C. R. Müller, F. Fayon, D. Massiot, A. Fedorov, C. Copéret, A. Lesage and P. Florian, *Chem. Mater.*, 2021, **33**, 3335–3348.



- 27 C. Coperet, A. Comas-Vives, M. P. Conley, D. P. Estes, A. Fedorov, V. Mougel, H. Nagae, F. Nunez-Zarur and P. A. Zhizhko, *Chem. Rev.*, 2016, **116**, 323–421.
- 28 K. Lee and S. B. Hong, *ACS Catal.*, 2019, **9**, 10640–10648.
- 29 W. Dai, X. Sun, B. Tang, G. Wu, L. Li, N. Guan and M. Hunger, *J. Catal.*, 2014, **314**, 10–20.
- 30 P. Tian, Y. Wei, M. Ye and Z. Liu, *ACS Catal.*, 2015, **5**, 1922–1938.
- 31 S. Ilias and A. Bhan, *ACS Catal.*, 2012, **3**, 18–31.
- 32 K. Horioka, K. Takahashi, N. Morimoto, H. Horiuchi, M. Akaogi and S. Akimoto, *Acta Crystallogr., Sect. B: Struct. Crystallogr. Cryst. Chem.*, 1981, **37**, 635–638.
- 33 B. K. Teo, *EXAFS: Basic Principles and Data Analysis*, Springer-Verlag, Berlin, Heidelberg, New York, Tokyo, 1986.
- 34 J. Timoshenko and A. Kuzmin, *Comput. Phys. Commun.*, 2009, **180**, 920–925.
- 35 A. Sadezky, H. Muckenhuber, H. Grothe, R. Niessner and U. Pöschl, *Carbon*, 2005, **43**, 1731–1742.
- 36 C. Wang, X. Zhao, M. Hu, G. Qi, Q. Wang, S. Li, J. Xu and F. Deng, *Angew. Chem., Int. Ed.*, 2021, **60**, 23630–23634.
- 37 P. Ferri, C. Li, C. Paris, A. Vidal-Moya, M. Moliner, M. Boronat and A. Corma, *ACS Catal.*, 2019, **9**, 11542–11551.
- 38 J. T. C. Wennmacher, S. Mahmoudi, P. Rzepka, S. Sik Lee, T. Gruene, V. Paunovic and J. A. van Bokhoven, *Angew. Chem., Int. Ed.*, 2022, **61**, e202205413.
- 39 J. P. Lange, A. Gutsze, J. Allgeier and H. G. Karge, *Appl. Catal.*, 1988, **45**, 345–356.
- 40 M. A. Callejas, M. T. Martínez, T. Blasco and E. Sastre, *Appl. Catal., A*, 2001, **218**, 181–188.
- 41 E. Koninckx, P. S. F. Mendes, J. W. Thybaut and L. J. Broadbelt, *Appl. Catal., A*, 2021, **624**, 118296.
- 42 E. A. Uslamin, H. Saito, N. Kosinov, E. Pidko, Y. Sekine and E. J. M. Hensen, *Catal. Sci. Technol.*, 2020, **10**, 2774–2785.

